

# Baroclinic energy cycles in two-layer quasi-geostrophic turbulence

Matthew Lobo

Program in Atmospheric and Oceanic Sciences, Princeton University, Princeton, NJ, USA Corresponding author: Matthew Lobo, mattlobo@princeton.edu

(Received 9 June 2025; revised 5 October 2025; accepted 6 October 2025)

We consider the two-layer quasi-geostrophic model with linear bottom friction and, in certain simulations, a planetary vorticity gradient,  $\beta$ . We derive energy budgets in wavenumber space for eddy available potential energy (EAPE), baroclinic eddy kinetic energy (EKE) and barotropic EKE, a particular decomposition that has previously been overlooked. The conversion between EAPE and baroclinic EKE,  $\widehat{T}^{W}$ , has a strong dependence on both bottom drag strength and planetary  $\beta$ . At the deformation scale  $\widehat{T}^{\widetilde{W}}$ is always negative, representing the conversion of EAPE to EKE via baroclinic instability. For strong, linear bottom drag,  $\widehat{T}^W$  is positive at large scales due to frictional energisation of the baroclinic mode, providing a large-scale EAPE source. With weak-to-moderate bottom drag and moderate-to-strong planetary  $\beta$ ,  $\widehat{T}^W$  is the dominant source of EAPE at large scales, converting baroclinic EKE that has experienced a baroclinic inverse cascade back into EAPE, and thus closing a novel and exclusively baroclinic energy loop. With planetary  $\beta$ , zonal jets form and the dominant large-scale processes in the energy cycle of the system, e.g. barotropic dissipation and the peak of positive  $\widehat{T}^W$ , occur at the meridional wavenumber corresponding to the jet spacing, with no zonal wavenumber component, i.e.,  $k_x = 0$ . Importantly, the traditional source of large-scale EAPE, barotropic stirring of the baroclinic mode, is not a part of this  $k_x = 0$  energy cycle, and thus plays a secondary role. The results suggest that consideration of horizontally two-dimensional processes is requisite to understand the energetics and physics of baroclinic geophysical jets.

**Key words:** quasi-geostrophic flows, stratified turbulence, jets

### 1. Introduction

The two-layer quasi-geostrophic (QG) model is a simple model of rotating and stratified fluids, often used as an idealised representation of the Earth's oceans (Thompson 2010;

Wang, Jansen & Abernathey 2016) and atmosphere (Larichev & Held 1995; Lee 1997), and gas giant atmospheres (Williams 1985). OG dynamics assume advective time scales that are long enough to be affected by planetary rotation, and length scales of the order of the deformation radius. The deformation radius essentially describes how far a baroclinic wave propagates before being affected by planetary rotation. A common configuration of the two-layer QG model in geophysical fluids is doubly periodic, with zonal (east-west) background flow and a planetary rotation parameter, f, that possibly varies linearly in the meridional (north-south) direction. Rossby waves form due to background potential vorticity (PV) gradients and the material conservation of PV (Rossby 1939; Panetta, Held & Pierrehumbert 1987), analogous to drift waves in a magnetised plasma (Hasegawa, Maclennan & Kodama 1979; Connaughton, Nazarenko & Quinn 2015). The choice of a constant background zonal flow is analytically convenient, and allows for the formation of turbulence that is representative of geophysical flows (e.g. Arbic & Flierl 2004; Thompson 2010). Time-mean zonal jets may form in the presence of meridional PV gradients (Panetta 1993; Thompson & Young 2007), thus providing a background state that compares favourably with patches in the ocean (Maximenko, Bang & Sasaki 2005; Sokolov & Rintoul 2007) and gas giant planets (Porco et al. 2003).

With zero prescribed background vorticity, baroclinic instability is the primary mechanism that supports unstable mode growth (Charney 1947; Eady 1949). The background interface slopes in the meridional direction due to thermal wind balance with the background zonal flow. For baroclinic instability to occur, two interacting baroclinic waves of the same lateral scale mutually reinforce each other. Once these growing baroclinic waves reach finite amplitude, geostrophic turbulence ensues. The growing baroclinic waves source energy from the assumed-infinite well of potential energy stored in the idealised, prescribed background sloping interface. We thus assume that the time scale required to add background potential energy to the background state from, for example, wind forcing, is much shorter than the time scale of the extraction of background potential energy by the perturbation flow. When this thermal damping rate is not much faster than the extraction of background potential energy, there may be oscillations between turbulent and quiescent flow regimes (Jougla & Dritschel 2017).

One of the hallmark characteristics of quasi-two-dimensional QG turbulence is an inverse cascade of kinetic energy, from smaller to larger scales (Salmon 1980). A particularly well-studied configuration of the two-layer QG model assumes a flat bottom on an f plane (i.e. no variations of the Coriolis parameter), equal layer thicknesses and weak linear bottom drag. In this configuration, essentially all of the kinetic energy inverse cascade occurs in the barotropic mode (Larichev & Held 1995), where the two-layer QG streamfunction is split into a depth-averaged 'barotropic' (BT) mode and a depth-dependent 'baroclinic' (BC) mode. The BC-BT dual cascade is the energy cycle where eddy available potential energy (EAPE), generated at large scales by BT flows, cascades forward to the deformation scale as, essentially, a passive tracer. At the deformation scale, EAPE is converted to BT eddy kinetic energy (EKE) via BC instability and nonlinear barotropisation, cascaded upscale as BT EKE, and then halted and dissipated due to a combination of background PV gradients (such as planetary vorticity or bottom topography) and bottom drag. We call this energy cycle the 'BC-BT' dual cascade because there is a forward cascade of EAPE and an inverse cascade of BT energy.

However, moderate-drag simulations have eddy characteristics that compare most favourably with the observed ocean (Arbic & Flierl 2004). In moderate-drag simulations there is a lack of total barotropisation at the deformation scale, and an inverse cascade of BC EKE also occurs (Scott & Arbic 2007), completing what we call the BC-BC dual cascade since there is a forward cascade of EAPE and an inverse cascade of BC EKE.

Once meridional variations of the Coriolis parameter are considered as  $f = f_0 + \beta y$  (the so-called planetary  $\beta$  plane), the inverse cascades are arrested at a scale set by the planetary vorticity gradient,  $\beta$ , where energy accumulates in the zero zonal wavenumber  $(k_x = 0)$  mode as zonal jets (Vallis & Maltrud 1993; Rhines 1994). Zonal jets act as barriers to meridional eddy fluxes (Panetta 1993; Ferrari & Nikurashin 2010), but enhance other processes such as the zonal dispersion of passive tracers (Holloway & Kristmannsson 1984; Smith 2005).

Most studies of two-layer QG turbulence use diagnostic energy budgets that are either decomposed by layer (Pudig & Smith 2025), decomposed by BT and BC modes (Larichev & Held 1995) or consist of total mechanical energy (Jansen & Held 2014), with each decomposition best suited for different applications. Lee (2010) considered an *x*-space (geographical-space) EAPE budget in the two-layer QG model. Section 9.8 of Vallis (2017) presents an EAPE to EKE conversion term, but does not pursue use of this term in model diagnostics. No study has considered either an EAPE budget in *k* space (wavenumber space), or separate budgets for EAPE, BC EKE and BT EKE. The *k*-space decomposition of EAPE, BC EKE and BT EKE offers a novel perspective on energy pathways (especially BC) in the two-layer model, as we will show.

We investigate energy cycles in the two-layer QG model as a function of bottom drag strength and planetary  $\beta$ . Section 2 provides an overview of the governing equations, energy diagnostics and numerical model. Section 3 presents analysis of simulation output with rigorous interpretation, providing novel insight into turbulent processes and energy pathways in the two-layer QG model. A brief summary, caveats and extensions of this work are discussed in § 4.

# 2. Methods

## 2.1. Model equations

The material time derivative of the total QG PV,  $q_k^{tot}$ , is balanced by small-scale dissipation (ssd) in both layers and linear drag in the lower layer

$$\frac{D_k}{Dt}q_k^{tot} = -\delta_{k\,2} \left(\kappa \nabla^2 \psi_k\right) + ssd,\tag{2.1}$$

for k = 1, 2 with k increasing downward,  $\delta_{k\,2}$  the Kronecker delta that is non-zero only for layer 2, and  $\psi_k$  the layer-wise perturbation streamfunction. The linear drag coefficient,  $\kappa$ , has dimensions of inverse time, with linear drag a basic representation of a bottom Ekman layer (Charney & Eliassen 1949). Small-scale dissipation is accomplished via the default exponential wavenumber cutoff filter in the numerical model code described in § 2.3 (see, also, LaCasce 1996). The material derivative advects with the total flow in the kth layer

$$\frac{\mathbf{D}_k}{\mathbf{D}t} \equiv \partial_t + (\boldsymbol{U}_k + \boldsymbol{u}_k) \cdot \nabla, \tag{2.2}$$

where  $U_k$  and  $u_k$  are the respective background and perturbation horizontal geostrophic velocity vectors for layer k. In general, uppercase symbols represent prescribed, background values while lowercase symbols denote perturbations.

The total QG PV is the sum of a prescribed, background component and perturbations about this background state

$$q_k^{tot} = Q_k + q_k. (2.3)$$

Background QG PV in the two layers is

$$Q_1 = 2 f_0 y S/H$$
, and  $Q_2 = -2 f_0 y S/H$ , (2.4)

where, through thermal wind balance, the prescribed interface slope is

$$S = f_0 U_1/g^{\mathsf{r}}. (2.5)$$

The resting thicknesses of the two layers are equal at H/2.

The reduced gravity at the interface is  $g^r = g (\rho_2 - \rho_1)/\rho_0$ , where  $\rho_0$  is a Boussinesq reference density, and  $\rho_k$  are the prescribed densities in the two layers. Perturbation QG PV in the two layers is

$$q_1 = \nabla^2 \psi_1 + 2 f_0 \eta / H$$
, and  $q_2 = \nabla^2 \psi_2 - 2 f_0 \eta / H$ , (2.6)

where the horizontal Laplacian is  $\nabla^2 = \partial_{xx} + \partial_{yy}$ , the relative vorticity is  $\zeta_k = \nabla^2 \psi_k$  and the perturbation to the sloping interface height is

$$\eta = f_0(\psi_2 - \psi_1)/g^{\mathsf{r}} = -2 \ f_0 \tau/g^{\mathsf{r}}. \tag{2.7}$$

We consider a modal decomposition throughout, where the depth-independent BT mode is  $\psi \equiv (\psi_1 + \psi_2)/2$  and the BC mode is  $\tau \equiv (\psi_1 - \psi_2)/2$ .

# 2.2. Diagnostic energy budgets

We now derive diagnostic energy budgets in k space for respective EAPE, BC EKE and BT EKE. The layer-wise QG vorticity equations are

$$\partial_t \nabla^2 \psi_1 + U_1 \partial_x \nabla^2 \psi_1 + \partial_x \psi_1 \beta + J(\psi_1, \nabla^2 \psi_1) = -f_0 A_1, \tag{2.8a}$$

$$\partial_t \nabla^2 \psi_2 + \partial_x \psi_2 \beta + J(\psi_2, \nabla^2 \psi_2) = -f_0 A_2, \qquad (2.8b)$$

where we have assumed  $U_2 = 0$  and  $\partial_{yy}U_1 = 0$ , and have split the streamfunction into background and perturbation components. The Jacobian operator is  $J(a, b) \equiv \partial_x a \partial_y b - \partial_y a \partial_x b$  (representing advection of the second argument when the first argument is a streamfunction). The ageostrophic divergence terms are

$$A_k \equiv \partial_x u_{ag,k} + \partial_y v_{ag,k}. \tag{2.9}$$

Since QG theory assumes that vertical velocities are at most  $\mathcal{O}(Ro)$ , with Ro the assumed-small parameter Rossby number, we expect divergences to be relatively small, but non-zero. Vertically integrating the upper-layer continuity equation gives

$$w_{3/2} = A_1 H/2, (2.10)$$

where  $w_{3/2}$  is the vertical velocity at the 3/2 (i.e. between layers 1 and 2) interface, and we have assumed a rigid lid and no Ekman dynamics at the surface. Vertical integration of the lower-layer continuity equation gives

$$w_b - w_{3/2} = A_2 H/2. (2.11)$$

The vertical velocity evaluated at the bottom is found using an Ekman layer bottom boundary condition

$$w_b \equiv \kappa H \nabla^2 \psi_2 / (2 f_0), \tag{2.12}$$

following Charney & Eliassen (1949). We also consider the interface height equation

$$\partial_t \eta + J(\psi_2, \eta) + \partial_x \psi_2 S = w_{3/2}. \tag{2.13}$$

All terms in the following three energy budgets are defined in table 1. The naming convention for energy budget terms is as follows. The letters for the terms are P for production of perturbation energy, T for transfer between the three energy types, R for

	Symbol	Name	Expression
BT EKE	$\widehat{EKE}_{BT}$	BT EKE	$ \mathbf{k} ^2  \psi_{\mathbf{k}} ^2 / 2$
	$\widehat{T}^L_{BC o BT}$	Linear barotropization	$U_1 \psi_{\pmb{k}}^{\dagger} (\partial_x \nabla^2 \tau)_{\pmb{k}} / 2$
	$\widehat{R}_{BT}$	Nonlinear BT inverse cascade	$\psi_{\pmb{k}}^\dagger \mathbf{J}_{\pmb{k}}(\psi,\ \nabla^2 \psi)$
	$\widehat{T}^{N}_{BC o BT}$	Nonlinear barotropization	$\psi_{\pmb k}^\dagger {\rm J}_{\pmb k}( au,\  abla^2 au)$
	$\widehat{D}_{BT}$	BT friction	$\kappa\psi_{\pmb k}^\dagger[\nabla^2(\psi-\tau)]_{\pmb k}/2$
BC EKE	$\widehat{EKE}_{BC}$	BC EKE	$ \mathbf{k} ^2  \tau_{\mathbf{k}} ^2 / 2$
	$-\widehat{T}^{W}$	EAPE to BC EKE transfer	$2 f_0 \tau_{\pmb k}^\dagger w_{3/2,\pmb k} / H$
	$\widehat{T}^L_{BT o BC}$	Linear barotropization	$U_1 \tau_{\pmb{k}}^{\dagger} (\partial_x \nabla^2 \psi)_{\pmb{k}}/2$
	$\widehat{R}^{KE}_{BC}$	Nonlinear BC inverse cascade	$ au_{\pmb{k}}^\dagger  { m J}_{\pmb{k}}( au, \;  abla^2 \psi)$
	$\widehat{T}^{N}_{BT  o BC}$	Nonlinear barotropization	$ au_{\pmb{k}}^\dagger  \mathbf{J}_{\pmb{k}}(\psi, \; \nabla^2  au)$
	$\widehat{D}_{BC}$	BC friction	$\kappa  \tau_{\pmb k}^\dagger  [\nabla^2 (\tau - \psi)]_{\pmb k}/2$
EAPE	$\widehat{EAPE}$	EAPE	$\lambda^{-2} \tau_k ^2/2$
	$\widehat{P}$	EAPE production	$2 f_0 S \tau_{\mathbf{k}}^{\dagger} (\partial_x \psi)_{\mathbf{k}} / H$
	$\widehat{T}^W$	EAPE to BC EKE transfer	$-2 f_0 \tau_{\pmb k}^\dagger w_{3/2,\pmb k} / H$
	$\widehat{R}^{PE}_{BC}$	Nonlinear BC cascade	$-\lambda^{-2} \tau_{k}^{\dagger}  \mathrm{J}_{k}(\psi,    au)$

Table 1. A guide for terms in the k-space EAPE (2.16), BC EKE (2.15) and BT EKE (2.14) budgets. All tendency terms have the units of energy per unit time,  $m^2s^{-3}$ . Note that the energy budgets require adding of the complex conjugate, c.c., of each of these terms.

nonlinear redistribution terms (which do not transfer energy between the three energy types, but only redistribute energy of a given type between scales, thus integrating to zero over all wavenumbers) and D for drag terms. Subscripts are either BC signifying the term describes BC energy only, BT signifying the term describes BT energy only or (when needed for clarification) BC and BT with an arrow in between signifying the direction of energy transfer between the two modes when the term has a positive value. For nonlinear redistribution terms, R, superscripts denote whether the nonlinear term is describing potential or kinetic energy. For transfer terms, T, the superscripts denotes whether the term is associated with linear (L), nonlinear (N) or vertical velocity-related (W) processes.

The BT EKE equation is  $-\psi_k^{\dagger}[(2.8a)+(2.8b)]_k/2 + \text{c.c.}$  where ()<sub>k</sub> denotes a two-dimensional Fourier transform, ()<sup>†</sup> represents the complex conjugate of a single term and c.c. implies taking a complex conjugate of every preceding term in the relevant expression. Thus, we Fourier transform the sum of the layer-wise vorticity equations, multiply by the negative complex conjugate of the BT streamfunction over 2,  $-\psi_k^{\dagger}/2$ , and add the complex conjugate of the whole expression, leading to

$$\partial_t \widehat{EKE}_{BT} = \widehat{T}_{BC \to BT}^L + \widehat{T}_{BC \to BT}^N + \widehat{R}_{BT} + \widehat{D}_{BT} + \widehat{ssd} + \text{c.c.}$$
 (2.14)

The widehat symbol,  $\widehat{()}$ , denotes that the term is a function of either two-dimensional wavevector  $\mathbf{k} = \mathbf{i} \ k_x + \mathbf{j} \ k_y$ , or wavevector magnitude,  $|\mathbf{k}|$ , with the specific meaning clear in a given context. When terms are a function of  $|\mathbf{k}|$ , we assume an isotropic spectrum and take shell integrals at each wavevector magnitude. The assumption of isotropy is not always

valid, and an exposition of anisotropy in the energy cycles is a major point of this study. Instead, we use isotropic spectra as traditional, visually digestible, and 'starting-point' representations of spectral energy budgets.

The BC EKE budget is derived analogously, as  $-\tau_k^{\dagger}[(2.8a)-(2.8b)]_k/2 + \text{c.c.}$ , giving

$$\partial_t \widehat{EKE}_{BC} = \widehat{T}_{BT \to BC}^L - \widehat{T}^W + \widehat{T}_{BT \to BC}^N + \widehat{R}_{BC}^{KE} + \widehat{D}_{BC} + \widehat{ssd} + \text{c.c.}$$
 (2.15)

The EAPE budget is defined as  $g^r \eta_k^{\dagger} [(2.13)]_k / H + \text{c.c.}$ , leading to

$$\partial_t \widehat{EAPE} = \widehat{P} + \widehat{R}_{BC}^{PE} + \widehat{T}^W + \widehat{ssd} + \text{c.c.}$$
 (2.16)

The nonlinear redistribution terms,  $\widehat{R}_{BT}$ ,  $\widehat{R}_{BC}^{KE}$  and  $\widehat{R}_{BC}^{PE}$ , will respectively equal zero when integrated over all wavenumbers. Thus, when integrated over all wavenumbers, the potential-kinetic conversion term,  $\widehat{T}^W$ , balances  $\widehat{P}$  in the EAPE budget. In general, EAPE production,  $\widehat{P}$ , occurs on much larger scales than potential-to-kinetic BC conversion,  $\widehat{T}^W < 0$ , due to the role of the forward cascade of EAPE,  $\widehat{R}_{BC}^{PE}$ . The linear transfer terms  $\widehat{T}_{BT \to BC}^L$  and  $\widehat{T}_{BC \to BT}^L$  cancel each other wavenumber by wavenumber. The nonlinear transfer terms  $\widehat{T}_{BT \to BC}^N$  and  $\widehat{T}_{BC \to BT}^N$  will not cancel each other wavenumber by wavenumber, but will cancel when integrated over all wavenumbers. In addition,  $\widehat{T}^W$  cancels itself out when one sums together the EAPE and BC EKE budgets. Thus the sum of the production term,  $\widehat{P}$ , and the two friction terms,  $\widehat{D}_{BC}$  and  $\widehat{D}_{BT}$ , will sum to zero when they are first respectively integrated over all wavenumbers.

The energy budget decomposition used in the present study extends previously described two-layer QG turbulence phenomenology. Salmon (1980) described triad interactions between combinations of BT and BC modes. Later studies (e.g. Larichev & Held 1995; Scott & Arbic 2007) refined the arguments of Salmon (1980) by deriving nonlinear energy budget terms that specifically accounted for triad interactions that conserve energy within the BT or BC mode. Scott & Arbic (2007) claim but do not prove which nonlinear terms correspond to EAPE versus BC EKE. Here, we specifically show that the nonlinear redistribution terms, R, conserve energy within given energy types, i.e. conserve energy within BC EKE and EAPE, respectively. Last, Salmon (1980) uses total energy and layer-wise enstrophy conservation to describe some turbulent phenomenology, an approach that is precluded when EAPE and BC EKE are separated as in the present study. Thus, although we cannot leverage the triad interaction phenomenology of Salmon (1980) in the present study, we have proven the previous claim of the respective conservation of EAPE and BC EKE by the nonlinear redistribution terms. In § 4 we briefly discuss how the simulated jets of the present study invalidate some assumptions of Salmon (1980) and offer insight into the BC inverse cascade.

The results of this study concerning EAPE energy cycles are general, since the EAPE budget arises regardless of how EKE is decomposed. One major point of the present study is the utility of decomposing the BC energy budget into respective budgets for EAPE and BC EKE. The traditional, total BC energy budget (see, e.g. Larichev & Held 1995; Thompson & Young 2006) is the sum of the EAPE and BC EKE budgets [(2.15) + (2.16)], leading to the cancellation of  $\widehat{T}^W$ , ambiguity in the effects of friction on BC energy, and less insight into the physics of the turbulence more generally. Crucially, by combining the budgets for EAPE and BC EKE one is not able to explain how BC EKE that experiences an inverse cascade is either barotropised or converted back into EAPE.

The potential-kinetic transfer term,  $\widehat{T}^W$ , describes a correlation between interface

The potential-kinetic transfer term,  $T^W$ , describes a correlation between interface vertical velocities,  $w_{3/2}$ , and the perturbation interface height,  $\eta$ . BC EKE is converted to EAPE when  $w_{3/2}$  acts to increase  $\eta$ , whereas EAPE to BC EKE conversion occurs when

the interface vertical velocity acts to flatten perturbations to the interface height. Thus the vertical velocity at the interface plays a central role in the present study. We diagnose  $w_{3/2}$  by eliminating the time derivatives from the vorticity and interface height equations as  $(f_0/g^r)[(2.8a)-(2.8b)] + \nabla \times (2.13)$ , producing an elliptic equation

$$(\nabla^2 - \lambda^{-2})w_{3/2} = f_0 \left[ \nabla^2 J(\psi_2, \ \psi_1) + J(\psi_2, \ f + \zeta_2) - J(\psi_1 + U_1 y, \ f + \zeta_1) \right] / g^{\mathsf{r}} - \lambda^{-2} w_b / 2 + \nabla^2 J(\psi_2, \ S y).$$
(2.17)

Using the relationships  $J(\tau, \nabla^2 \psi) = [J(\psi_1, \nabla^2 \psi_1) - J(\psi_2, \nabla^2 \psi_1) + J(\psi_1, \nabla^2 \psi_2) - J(\psi_2, \nabla^2 \psi_2)]/4$  and  $\nabla^2 J(\psi_2, \psi_1) = J(\psi_2, \nabla^2 \psi_1) - J(\psi_1, \nabla^2 \psi_2)$  the equation for  $w_{3/2}$  (2.17) is written

$$(\nabla^2 - \lambda^{-2})w_{3/2} = -f_0[4J(\tau, \nabla^2\psi) + 2J(\tau, f) + J(U_1y, \nabla^2\psi) + 2f_0w_b/H]/g^{\mathsf{r}}.$$
(2.18)

The deformation radius,  $\lambda$ , in the two-layer system with equal layer thicknesses satisfies  $\lambda^{-2} = 4 f_0^2/(H g^r)$ . Equation (2.18) is a form of the omega equation (Hoskins, Draghici & Davies 1978; Pinot, Tintoré & Wang 1996; Hoskins, Pedder & Jones 2003). In a doubly periodic domain, (2.18) is solved spectrally.

# 2.3. Numerical model and model parameters

We use the GeophysicalFlows.jl model (Constantinou *et al.* 2021) whose multilayer configuration is optimised for execution on GPU. The square domain, with side lengths  $L_x = L_y = 50\pi\lambda$  and  $1024 \times 1024$  grid points, has a resolution of  $\Delta x = \Delta y = 0.15\lambda$ . The deformation radius is  $\lambda = 28$  km and the total depth is H = 4 km. The upperand lower-layer background flows are  $U_1 = 0.01$  and  $U_2 = 0.0$  m s<sup>-1</sup>, respectively. The Coriolis parameter is  $f_0 = 8.3e - 5$  s<sup>-1</sup> and the dimensionless planetary vorticity gradient  $\beta^* \equiv \beta \lambda^2/U$  is varied between 0 and 0.75. The dimensionless linear drag coefficient  $\kappa^* \equiv \kappa \lambda/U$  is varied in the range 0.25 to 4.0. The background velocity scale is set as  $U \equiv U_1/2$ , since this gives a critical  $\beta^*$  value of unity. Small-scale dissipation occurs via the default wavenumber cutoff filter of the model code. We run each simulation to  $t^* = t(U/\lambda) = 300$  eddy periods, long enough for an energetic steady state to emerge for all parameters considered here. We then run the simulation for another 100 eddy periods, calculating diagnostics online with a period of  $\Delta t^* = 0.01$ .

## 3. Simulation output

Weak-drag ( $\kappa^* = 0.25$ ) and strong-drag ( $\kappa^* = 4.0$ ) regimes of f-plane QG turbulence are defined based on the dominant processes being the BC-BT dual cascade, or BC-BT and BC-BC dual cascades plus a conversion of BC EKE to EAPE at large scales, respectively. After investigating drag-dependent energy cycles on an f plane, we show that a closed BC energy loop forms in the presence of planetary  $\beta$  and weak drag. We do not consider both strong drag and strong planetary  $\beta$ , as strong drag inhibits jet formation (Berloff *et al.* 2011), and leads to a complicated relationship between  $\kappa^*$ ,  $\beta^*$  and turbulent characteristics.

# 3.1. Varying drag strength

For weak drag, the traditional BC-BT dual cascade, as illustrated in figure 1(a), prevails (figure 2a-c). EAPE is produced at large scales and cascaded forward, where it is converted to BC EKE at a range of deformation-scale wavenumbers. At these same deformation-scale wavenumbers BC EKE is converted to BT EKE via nonlinear barotropisation. BT EKE is then cascaded upscale where it is ultimately halted

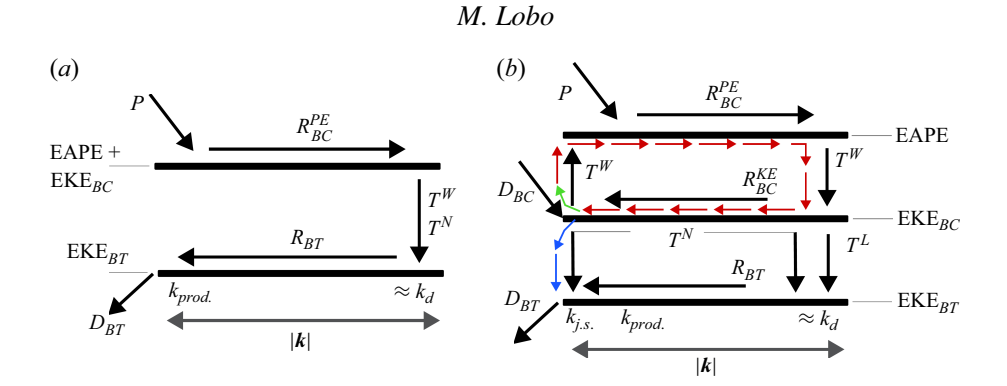


Figure 1. (a) The energy cycle diagram used by Salmon (1980) and Thompson & Young (2006), among others. See the beginning of § 3.1 for a description of the energy pathways. Here,  $k_{prod}$  denotes the scale of EAPE production via  $\widehat{P}$  and  $k_d$  denotes the deformation scale where EAPE is converted to BT EKE in Salmon (1980) and others. (b) An energy cycle diagram, modified from Salmon (1980), to include a separate BC EKE reservoir. Frictional effects  $(\widehat{D}_{BC})$  add EKE that is immediately converted to EAPE via  $\widehat{T}^W$  at large scales. In the strong-drag, f-plane case, once the energy undergoes an inverse cascade (red arrows), it is barotropised and dissipated as BT EKE (blue arrows). Thus there is no purely BC energy loop. In the weak-drag, strong- $\beta^*$  case, the main source of large-scale EAPE,  $\widehat{T}^W$ , is energised both via frictional effects and the inverse cascade of BC EKE. With the BC inverse cascade feeding energy into large-scale kinetic-to-potential energy conversion (green arrow), there is a closed loop of purely BC energy. Approximately half of the BC EKE that experiences an inverse cascade is still barotropised (blue arrows). Note that, as a modification to panel (a), the largest scales in panel (b) are set by the jet-spacing scale,  $k_{i,s}$ , rather than the EAPE production scale,  $k_d$ . Dissipation is generally strongest at the largest energy-containing scales, i.e.  $k_{prod}$  in panel (a) and  $k_{j,s}$  in panel (b). For all symbols, we neglect the widehats for visual clarity. Note that, here, we follow, e.g. Roullet et al. (2012) and do not include either (i) the forward cascade of enstrophy, or (ii) the scale where the redistribution terms change sign, i.e. the injection scale. This choice is for visual clarity. See the end of § 3.2 for a discussion on the energy injection scale in the present set of simulations.

and dissipated by friction. Note that the high-wavenumber, broadband processes in figure 2(a-c) have small amplitudes but still integrate to values comparable to the sharp peaks at low wavenumbers. In x space, weak-drag, f-plane turbulence falls into the vortex gas regime (Gallet & Ferrari 2020), where large-scale energy is organised into coherent vortices (figure 3a) that interact with one another to produce EAPE via  $\widehat{P}$  (figure 3b). In addition, here, we show that the vortices locally add EAPE via frictional effects (figure 3c), although this process is weak on the flat-bottom f plane.

For strong drag (figures 2d-2f), inviscid BC production,  $\widehat{P}$ , shifts to smaller scales, in accordance with a smaller arrest scale of the inverse cascade. In particular, the frictional arrest scale is found by setting the inverse time scale from the linear drag coefficient equal to a root mean square velocity scale over a length scale, and solving for the length scale,  $L_{\kappa} \equiv U_{rms}/\kappa$ . The most distinct feature in the strong-drag regime is that  $\widehat{T}^W$  now represents a modest source of EAPE at large scales, remaining a sink at the deformation scale. From figures 2(d) and 2(e), it is unclear whether  $\widehat{T}^W$  is energised via frictional processes ( $\widehat{D}_{BC}$ ) or the BC inverse cascade ( $\widehat{R}_{BC}^{KE}$ ). For this to be a closed BC energy loop, some of the energy going into  $\widehat{T}^W$  has to come from the BC inverse cascade.

Coherence between two signals tells us how much they are correlated in x space at a given wavevector, and is defined as

$$C(A, B; \mathbf{k}) = \frac{\sum_{n=1}^{N} A_{\mathbf{k}} B_{\mathbf{k}}^{\dagger} \sum_{n=1}^{N} A_{\mathbf{k}}^{\dagger} B_{\mathbf{k}}}{\sum_{n=1}^{N} A_{\mathbf{k}} A_{\mathbf{k}}^{\dagger} \sum_{n=1}^{N} B_{\mathbf{k}} B_{\mathbf{k}}^{\dagger}},$$
(3.1)

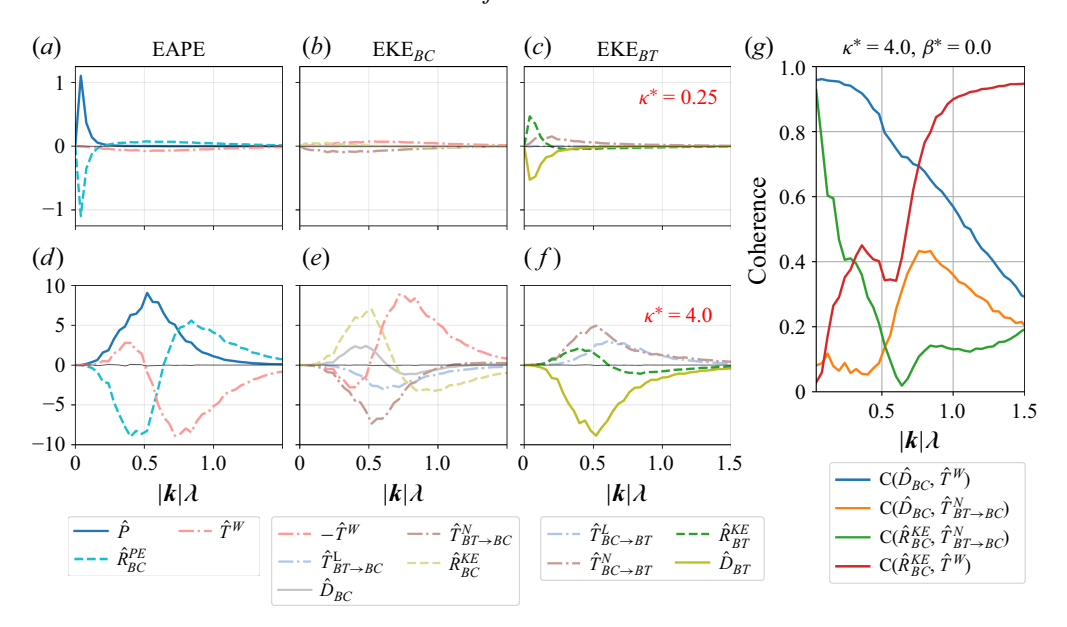


Figure 2. (a–f) Energy tendency terms (see table 1) as a function of  $|\mathbf{k}|\lambda$  for (left column) EAPE, (middle-left column) BC EKE and (middle-right column) BT EKE, all with  $\beta^* = 0$ . We consider (top row) weak drag at  $\kappa^* = 0.25$  and (bottom row) strong drag at  $\kappa^* = 4.0$ . All terms are normalised by  $U_{BT}^3 \lambda^{-1}$  where  $U_{BT}$  is the time- and domain-average root mean square BT velocity. Solid lines are sources or sinks of total perturbation energy, dashed lines transfer energy within modes and dot-dashed lines transfer energy between modes. The thin black lines are residuals. (g) Isotropic coherence of large-scale sources and sinks of BC EKE.

where  $N=10^4$  is the number of snapshots that we use for the diagnostics. All coherences that we show are mean values computed using shell integrals over wavevector magnitude, and are thus assumed isotropic. We are interested in large-scale BC EKE transfer for the f-plane, strong-drag case, so that we calculate all pairs of  $\widehat{R}_{BC}^{KE}$  and  $\widehat{D}_{BC}$  (positive terms at large scales) with  $\widehat{T}^W$  and  $\widehat{T}_{BT\to BC}^N$  (negative terms at large scales; figure 2e). Figure 2(g) shows that  $C(\widehat{D}_{BC}, \widehat{T}^W)$  is large at relatively low |k|, signifying that frictional energisation  $(\widehat{D}_{BC})$  is a source of BC EKE that is converted to EAPE via  $\widehat{T}^W$ . At relatively high |k|,  $C(\widehat{D}_{BC}, \widehat{T}^W)$  drops while  $C(\widehat{R}_{BC}^{KE}, \widehat{T}^W)$  increases due to BC instability  $(\widehat{T}^W < 0)$  feeding the inverse cascade of BC EKE. At relatively low |k|, the coherence between the two nonlinear processes  $C(\widehat{R}_{BC}^{KE}, \widehat{T}_{BT\to BC}^N)$  is large, signifying large-scale barotropisation of BC EKE that has undergone the inverse cascade. Lastly,  $C(\widehat{D}_{BC}, \widehat{T}_{BT\to BC}^N)$  is small at low |k|, signifying that energy produced via frictional effects is not directly barotropised. These coherences reveal the BC energy pathways: frictionally generated BC EKE is converted to EAPE via  $\widehat{T}^W$ , while BC EKE that reaches large scales via an inverse cascade is barotropised via nonlinear processes. Thus while frictional effects act to energise EAPE, there is no closed BC energy cycle. The red plus blue arrows in figure 1(b) show these results schematically.

# 3.2. Enhancement of baroclinic cycle by planetary $\beta$

The drag strength required for  $\widehat{T}^W > 0$  at large scales to manifest on the flat-bottom f plane is  $\kappa^* \approx 2.0$  (not shown), which is larger than is expected to be valid for the observed ocean (Arbic & Flierl 2004). We now consider how the inclusion of planetary  $\beta$  at weaker drag values affects the BC energy cycle.

#### (a) (b) (c) $\kappa^* = 0.25, \, \beta^* = 0.0$ 25 EKE<sub>BT</sub> $D_{BC}$ 20 $y/2\pi\lambda$ 15 10 5 0 20 25 5 10 20 25 25 10 15 0 15 5 10 15 20 (f)(d) $\kappa^* = 0.25, \, \beta^* = 0.75$ 25 EKE<sub>BT</sub> $D_{BC}$ 20 $y/2\pi\lambda$ 15

M. Lobo

Figure 3. Snapshots of (a,d) BT EKE, (b,e) EAPE production and (c,f) frictional effects on the BC mode for (top row) the weak-drag f plane, and (bottom row) the weak-drag  $\beta$  plane. All panels are normalised by the respective maximum absolute value, with colour bar limits of -1 (blue) to 1 (red). The strong, narrow bands of BT EKE in panel (d) are associated with strong eastward jets. Panel (d) denotes the jet scale,  $L_j$ , and jet-spacing scale,  $L_j$ ,  $L_j$ .

10 15 20

 $x/2\pi\lambda$ 

10

15 20

 $x/2\pi\lambda$ 

25

For weak drag and weak  $\beta^*$  (figure 4a–c) BC-BT dual-cascade phenomenology dominates. However, for  $\beta^*=0.75$  the dominant source of large-scale EAPE is  $\widehat{T}^W$  (figure 4d). It is remarkable that inviscid BC energy production,  $\widehat{P}$ , does not possess the same sharp peak as almost every other term in the budget (figure 4d–f). Two-dimensional spectra of energy tendency terms show that, while  $\widehat{P}$  is limited to zonal scales that are strictly smaller than the jet scale ( $k_x\lambda\approx0.5$ ; figure 5d), no such limit exists for  $\widehat{T}^W$  and  $\widehat{R}^{PE}_{BC}$  in the EAPE budget (figures 5e–5f). Since  $\widehat{P}$  depends on the meridional BT velocity that takes the form of zonally oriented waves, the jet scale,  $L_j$ , i.e. the zonal wavelength of the Rossby waves that make up the strong eastward jet systems (figure 3d), limits the scale of inviscid BC production. Such zonal orientation of  $\widehat{P}$  is clear in x space (figure 3e), where it is shown that the spatial distribution of  $\widehat{P}$  is characterised by oscillations with a zonal wavenumber that is, at maximum, the zonal wavenumber of the jets in figure 3(d).

On the other hand, processes that are isotropic on the f plane (such as  $\widehat{T}^W$  and  $\widehat{R}^{PE}_{BC}$  in figures 5b-c) develop relatively uninhibited in the zonal direction on the  $\beta$  plane, while occurring along jets in the meridional direction. Thus their two-dimensional wavenumber spectra have large peaks with  $k_x = 0$ ,  $k_y \lambda \approx 0.5$  (figures 5e-f), where the meridional wavenumber  $k_y$  is set by the jet-spacing scale,  $L_{j.s.}$  (figure 3d). The peaks at  $k_x = 0$  in figures 5(e)-(f) are thus the source of the large-scale peaks found in the isotropic spectra in figure 4(d). Similarly, the large-scale peaks in figures 4(e) and 4(f) are associated with strong processes that have  $k_x = 0$ . The frictional effects on the BC mode (diagnosed via  $\widehat{D}_{BC}$ ) are an example of a process that develops relatively unimpeded in the zonal direction

10

10 15 20

 $x/2\pi\lambda$ 

25

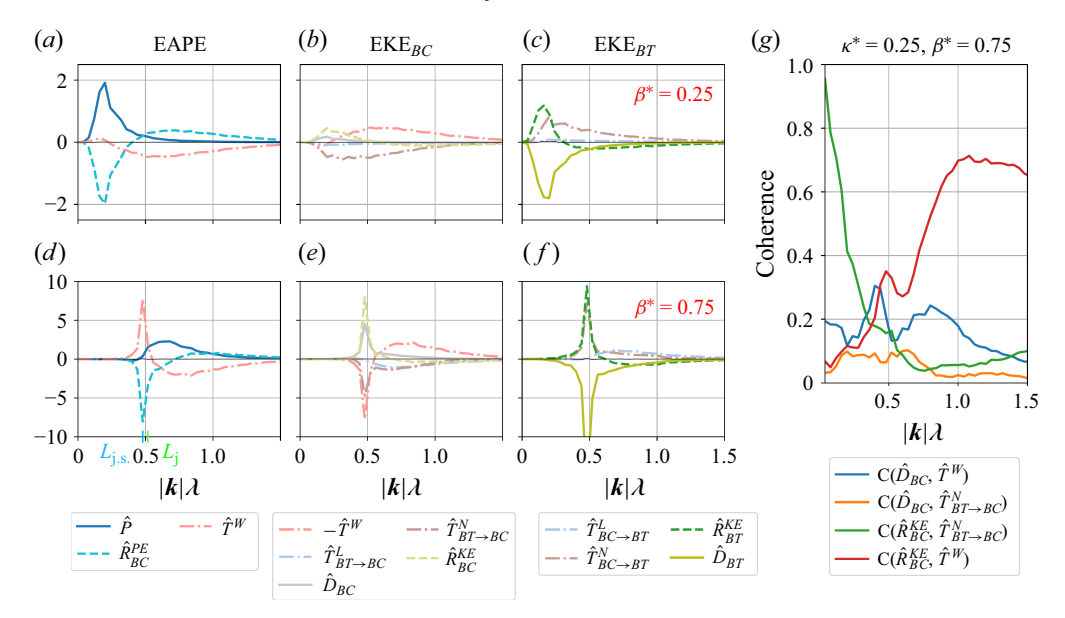


Figure 4. (*a*–*f*) Energy tendency terms (see table 1) as a function of  $|\mathbf{k}|\lambda$  for (left column) EAPE, (middle-left column) BC EKE and (middle-right column) BT EKE, all with  $\kappa^* = 0.25$ ; for (top row)  $\beta^* = 0.25$  and (bottom row)  $\beta^* = 0.75$ . All terms are normalised by  $U_{BT}^3\lambda^{-1}$  where  $U_{BT}$  is the time- and domain-average root mean square BT velocity. (*g*) Isotropic coherence of large-scale sources and sinks of BC EKE.

(figure 3f). That is, even though frictional energisation still has some zonal structure, this zonal structure roughly oscillates about a large zonal mean value that contributes most to the total value of  $\widehat{D}_{RC}$ .

Frictional processes (and all other processes with sharp peaks at the jet-spacing scale) are tied to the jet dynamics and are concentrated in the jet cores, and thus appear in diagnostics at a meridional wavenumber that reflects the jet-spacing scale,  $L_{j.s.}$  (see figure 3d). It is noteworthy that BT dissipation occurs at the same scale as EAPE production on the isotropic f plane (figure 2), while BT dissipation largely occurs at a scale set by the jets on the  $\beta$  plane with strong jets (figure 4f). This shows that the energy sink of the  $k_x = 0$  energy cycle is drag on the strong eastward jets.

Most of the EAPE generated via  $\widehat{P}$  is converted to BC EKE via  $\widehat{T}^W$  without undergoing a forward cascade (figures 5d and 5e). The inverse BC EKE cascade (green line in figure 4e) and frictional energisation (grey line in figure 4e) both inject BC EKE at large scales. Large-scale BC EKE must either be barotropised or converted back into EAPE via  $\widehat{T}^W$ . In fact, since  $\widehat{D}_{BC}$  is not large enough alone to balance  $\widehat{T}^W$  at large scales in figure 4(e), the nonlinear inverse cascade of BC EKE must also contribute to the flux of BC EKE back into EAPE via  $\widehat{T}^W$ . In addition, the higher-wavenumber values at  $k_x = 0$ ,  $k_y \lambda \approx 1.0$  in figures 5(e)–(f) are associated with energetic processes on the flanks of the jets, akin to the momentum convergences in Thompson & Young (2007), and thus occur with a meridional wavelength of approximately half of the jet-spacing scale.

The two nonlinear processes are coherent at large scales (green line in figure 4g), suggesting that much of the BC EKE that experiences the inverse cascade is barotropised. However, both  $\widehat{D}_{BC}$  and  $\widehat{R}_{BC}^{KE}$  are coherent with  $\widehat{T}^W$  (blue and red lines in figure 4g, respectively), offering further evidence that both of the former energy tendency terms contribute to the large-scale source of EAPE,  $\widehat{T}^W$ . In fact, conversion of BC EKE to

# M. Lobo

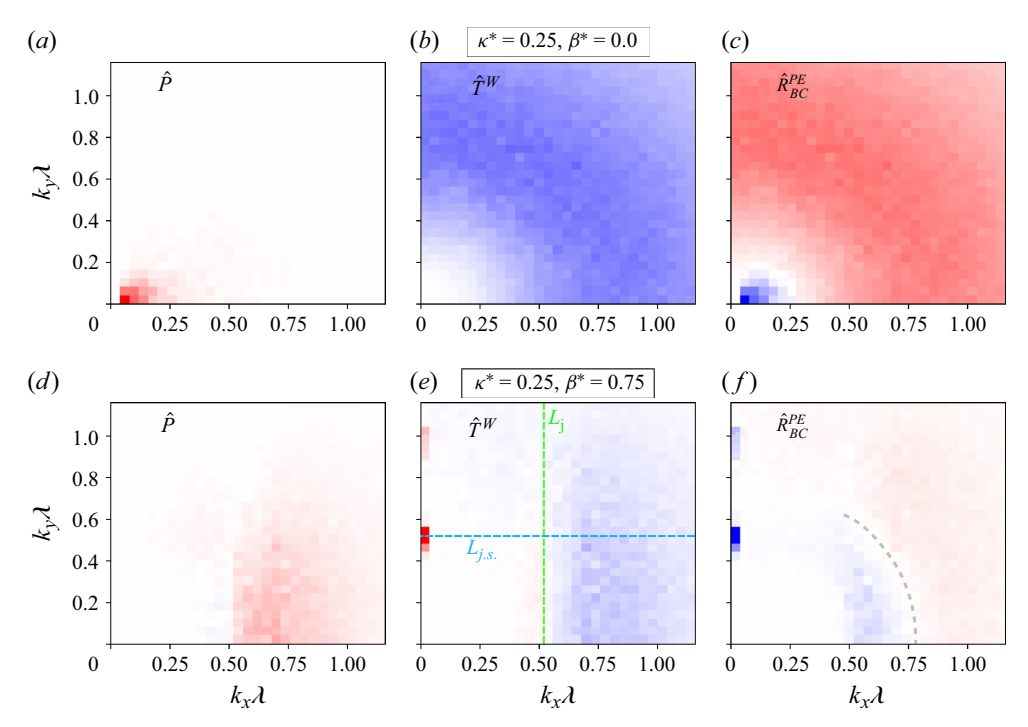


Figure 5. Time averages of two-dimensional EAPE budget terms for (top row) the weak-drag f plane, and (bottom row) the weak-drag  $\beta$  plane. Panels (a-c) are normalised by the maximum value, with colour bar limits of -1 (blue) to 1 (red). Panels (d-f) are normalised by one quarter of the maximum value. Otherwise the only features that show are the sharp peaks at  $k_x = 0$ . We multiply all terms by  $|\mathbf{k}|$  to visualise high-wavenumber values. Panel (e) also shows the wavenumbers corresponding to the jet scale,  $L_j$ , and the jet-spacing scale,  $L_{i,s}$ . In panel (f) we show the approximate energy injection wavenumber with the grey-dashed line.

EAPE is the largest sink of large-scale BC EKE, as opposed to barotropisation (figure 4e). Thus planetary  $\beta$  makes the BC inverse cascade a large-scale source of energy for  $\widehat{T}^W$ , closing a purely BC energy loop (red and green arrows in figure 1b).

Lastly, a feature of the energy budget spectra (figures 2 and 4) not shown in the idealised turbulent energy cycle diagrams (figure 1) is the length scale where the redistribution terms change sign, also known as the energy injection scale (Scott & Wang 2005). The energy injection scale is approximately the same for EAPE, BC EKE and BT EKE in the weakdrag, weak- $\beta^*$  case (figure 4a-c). However, the energy injection scale for EAPE is notably smaller than the energy injection scale for BC EKE and BT EKE in the weak-drag, strong- $\beta^*$  flow (figure 4d-f). The smaller injection scale for EAPE is due to the inviscid EAPE source, P, that creates EAPE at smaller scales than the jet-spacing scale. In fact, the EAPE injection scale in figure 4(d) ( $|k|\lambda \approx 0.75$ ) is seen as the transition from negative to positive values in the two-dimensional spectrum of  $\widehat{R}_{BC}^{PE}$  for zonal wavenumbers higher than the jet scale,  $k_x \lambda \ge 0.5$  (the EAPE injection scale is denoted by the grey-dashed line in figure 5f). Thus our simulations show that while the EAPE injection scale is set by the highestwavenumber EAPE source (in this case inviscid EAPE production, P), the BC EKE and BT EKE injection scales are set by the dominant  $k_x = 0$  jet-spacing-scale energy cycle. Further work might thus focus on the two-dimensional structure of the energy injection scale, since we have shown here that this scale is anisotropic for EAPE.

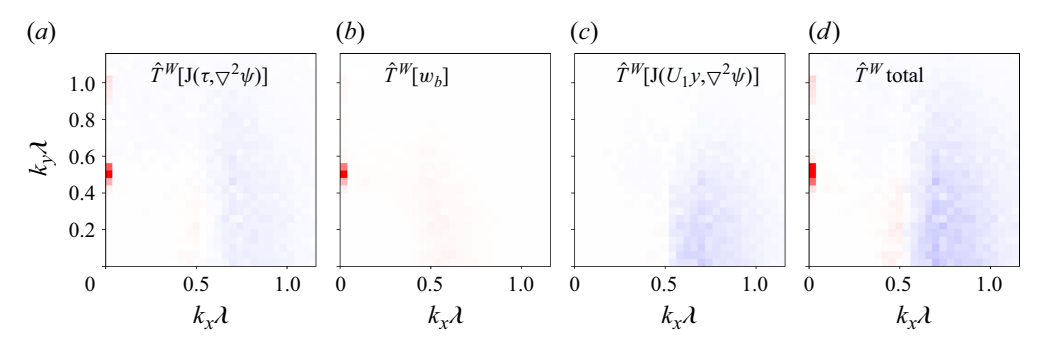


Figure 6. (a-c) The terms in decomposition of the potential-kinetic energy transfer term from (3.3). The contribution to  $\widehat{T}^W$  from  $\widehat{T}^W[J(\tau, f)]$  is negligibly small and is not shown. (d) The total potential-kinetic energy transfer term, which is the sum of panels (a)-(c). Note that panel (d) is exactly the same term as shown in figure 5(e). All terms are multiplied by  $|\mathbf{k}|$  to visualise the smaller values at high wavenumbers. All panels share a colour scale, with lower and upper limits of minus and plus one quarter of the maximum absolute value of the total conversion term,  $\pm max\{|\widehat{T}^W|\}/4$ .

# 3.3. Mechanics of large-scale kinetic-to-potential energy conversion

Although we have shown that the BC inverse cascade and frictional energisation add BC EKE to the large scales where the kinetic-to-potential energy conversion occurs, the mechanics of this energy conversion remain unclear. That is, although figure 4(e) shows that, for example, the BC inverse cascade deposits BC EKE at large scales, and figure 4(g) shows that the BC inverse cascade diagnostic term is coherent with the kinetic-to-potential conversion term, a mechanism for this energy conversion is yet to be proposed. To understand the mechanics of the correlation between  $w_{3/2}$  and  $\eta$ , we now decompose the diagnosed  $w_{3/2}$  (2.18) into separate components associated with different physical processes, and then look at how each of these contributions to  $w_{3/2}$  are correlated or anticorrelated to  $\eta$  in two-dimensional wavenumber space.

Since (2.18) is linear, the vertical velocity at the interface can be decomposed into the contributions from the different terms on the right-hand side as

$$w_{3/2} = w_{3/2} \left[ J(\tau, \nabla^2 \psi) \right] + w_{3/2} \left[ J(\tau, f) \right] + w_{3/2} \left[ U_1 \partial_x \nabla^2 \psi \right] + w_{3/2} \left[ w_b \right], \tag{3.2}$$

where the square brackets denote a functional dependence. Going one step further, we decompose  $\widehat{T}^W$  into contributions from the different  $w_{3/2}$  components

$$\widehat{T}^{W} = \widehat{T}^{W} \left[ J(\tau, \nabla^{2} \psi) \right] + \widehat{T}^{W} \left[ J(\tau, f) \right] + \widehat{T}^{W} \left[ U_{1} \partial_{x} \nabla^{2} \psi \right] + \widehat{T}^{W} \left[ w_{b} \right]. \tag{3.3}$$

This decomposed form of  $\widehat{T}^W$  is derived in an analogous way to the energy budgets in § 2.2.

The contribution from  $\widehat{T}^W[J(\tau, f)]$  is negligible (not shown). The BC advection of the BT vorticity,  $J(\tau, \nabla^2 \psi)$ , is associated with the inverse cascade of BC EKE,  $\widehat{R}^{KE}_{BC}$  (table 1). Here,  $\widehat{T}^W[J(\tau, \nabla^2 \psi)]$  contributes to both the jet-spacing-scale addition of EAPE at  $k_x = 0$  and the conversion of potential to kinetic energy at  $k_x \lambda \ge 0.5$  (figure 6a). In addition,  $\widehat{T}^W[J(\tau, \nabla^2 \psi)]$  is the sole contributor to the  $k_x = 0$ ,  $k_y \lambda \approx 1.0$  conversion of kinetic to potential energy that occurs on jet flanks. These results are consistent with  $\widehat{R}^{KE}_{BC}$  depositing BC EKE at large scales, where the BC EKE is then converted back into EAPE. Note, however, that even though a strong BC inverse cascade occurs for the strong-drag flow (figure 2e), there is not a dominant amount of large-scale BC EKE to EAPE conversion. Thus, in addition to a strong inverse cascade of BC EKE, the kinetic-to-potential energy conversion requires jets, which occur in the presence of planetary  $\beta$ .

The component of bottom velocity-dependent potential-kinetic energy conversion,  $\widehat{T}^W[w_b]$ , converts BC EKE to EAPE at large scales (figure 6b), consistent with  $\widehat{D}_{BC}$  only acting at large scales (figure 4e). On the other hand, background advection of BT vorticity,  $J(U_1y,\nabla^2\psi)$ , which is associated with linear barotropisation,  $\widehat{T}^L$  (table 1), only supports vertical velocities that convert potential to kinetic energy at the deformation scale (figure 6c). This result links the conversion of EAPE to BC EKE,  $\widehat{T}^W[U_1\partial_x\nabla^2\psi]$ , to the conversion of BC EKE to BT EKE,  $\widehat{T}^L$ , and thus provides new insight into barotropisation. That is, we have shown that a component of barotropisation that, strictly speaking, only describes a conversion of BC to BT EKE in the energy budgets ( $\widehat{T}^L$ ) is mechanistically linked to the conversion of EAPE to BC EKE via BC instability (described by  $\widehat{T}^W$  at the deformation scale).

## 4. Conclusion

In this study we presented two-layer QG energy budgets that treat EAPE and BC EKE separately. There is a term,  $\widehat{T}^W$ , that describes deformation-scale BC instability and, possibly, a conversion of BC EKE to EAPE at large scales. The value of  $\widehat{T}^W$  becomes positive at large scales (corresponding to the conversion of BC EKE to EAPE) due to either strong, linear bottom drag or weak drag and planetary  $\beta$ . With strong, linear bottom drag, there is a prominent BC inverse cascade. However, the source of kinetic to potential energy conversion is frictional energisation of BC EKE, and there is no closed BC energy loop (red plus blue arrows in figure 1b). With planetary  $\beta$ , zonal jets enhance weak-drag frictional energisation and also support a transfer of BC EKE to EAPE from the BC EKE inverse cascade, creating a closed-loop, purely BC energy cycle (red plus green arrows in figure 1b). Thus, zonal jets are required for the inverse cascade of BC EKE to feed into large-scale conversion of kinetic to potential energy.

Inviscid EAPE production, i.e. the EAPE source due to BT stirring of the BC mode, relies on the meridional BT velocity and is oriented zonally. Here, zonal orientation is characterised by oscillations with wavevectors that have a low-wavenumber cutoff of their zonal wavenumber component (i.e. has  $2\pi/k_x < L_j$  where  $L_j$  is the wavelength of a typical zonal Rossby wave; see figure 3e). Thus, it is the jet scale,  $L_j$  (i.e. the zonal Rossby wave length scale), rather than the jet-spacing scale,  $L_{j.s.}$  (i.e. the meridional distance between adjacent jets), that limits the length scale of inviscid BC production (figure 3d visualises these length scales). This limitation is illustrated by the two-dimensional wavenumber spectrum of the inviscid EAPE production term, which is dominated by values that have  $k_x \lambda > 0.5$  (figure 5d).

However, processes that are isotropic on the f plane, i.e. that do not rely on meridional velocities, develop relatively unimpeded in the zonal direction in the presence of jets on the  $\beta$  plane. In addition, these processes occur along the energetic eastward jets. Thus, most energy tendency terms have strong peaks at purely meridional wavenumbers corresponding to the jet-spacing scale, with  $k_x = 0$ . This can be seen, for example, in the two-dimensional spectra of  $\widehat{T}^W$  and  $\widehat{R}^{PE}_{BC}$  (figure 5e-f), with analogous results for the other terms. In addition, we have shown that the energy injection scale for EAPE is anisotropic in the presence of zonal jets. These results highlight the importance of the jet-spacing scale, a meridional length scale that is not as readily predicted as the jet scale (Thompson 2010), for turbulent energy cycles in the two-layer QG model with jets.

Roullet *et al.* (2012) used a QG model with higher vertical resolution to show an EAPE energy cycle that is similar to the one shown here. In addition, large-scale conversion of kinetic to potential energy has been diagnosed in a realistic ocean model (Wang *et al.* 2019) and a hierarchy of idealised models (Dettmer & Eden 2025). Thus processes

investigated in the present study may have analogues in QG energy cycles with more complex vertical structure (likely dependent on the vertical structure of background PV gradients; Lobo, Griffies & Zhang 2025), and more comprehensive models of ocean turbulence. Lee (2010) found that frictional energisation is an enhancement of inviscid EAPE production. However, here we have shown that frictional energisation acts at a very different horizontal wavevector than inviscid EAPE production, and requires further study. The ability to predict the large-scale production of potential energy (Larichev & Held 1995; Held & Larichev 1996) has seen recent progress (Gallet & Ferrari 2020). However, Gallet & Ferrari (2020) and others assume that the only large-scale source of EAPE is BT stirring of the BC mode. The present study suggests that this approach to estimating large-scale EAPE production is possibly an underestimate in the presence of geophysical jets. In particular, we plan to investigate whether there are x space arguments similar in spirit to those of Thompson & Young (2006) and Gallet & Ferrari (2020) that apply to energy cycles in strong jets in the two-layer QG model.

In a similar vein, Smith & Vallis (2002) showed that planetary  $\beta$  decreases baroclinicity in their simulations, consistent with statistical mechanical arguments (Venaille, Vallis & Griffies 2012). Here, we have shown strong jets in the presence of planetary  $\beta$  increase the BC inverse cascade, and thus increase the amount of large-scale BC EKE. On the other hand, Smith & Vallis (2002) do not mention the possibility of jet formation. In addition, Salmon (1980) describes the phenomenology of barotropisation by assuming that the largest-scale energy is at much larger scales than the deformation scale. Here we have shown that the inverse cascade processes occur along jets, on scales that are not much larger than the deformation scale, at least in the meridional direction. Thus two-layer QG turbulence with jets is categorically distinct from classic two-layer QG turbulence phenomenology. Future work will focus on reconciling the results of Smith & Vallis (2002) and the present study, as well as considering two-layer QG turbulence phenomenology in the presence of jets. We conjecture that while the catalytic role of  $\beta$  in barotropisation leads to more BT flow, the dynamic role of  $\beta$  in supporting jet formation can lead to more BC flow.

A major result of the present study is that, in addition to barotropisation, large-scale BC EKE can be converted back into EAPE. BC EKE experiences an inverse cascade in the observed ocean (Scott & Wang 2005; Storer et al. 2023) and ocean reanalysis products (Li & Xu 2021), and it is traditionally assumed that the inverse cascade is 'one way,' i.e. all energy that experiences an inverse cascade must be dissipated (see, e.g. § 5.3 of Ferrari & Wunsch 2009). Inverse cascades also occur on gas giants such as Jupiter (Young & Read 2017). We have demonstrated that, in the two-layer QG model, kinetic energy that experiences an inverse cascade can be recycled into potential energy, particularly in the presence of jets, which are common in the ocean (Maximenko et al. 2005; Sokolov & Rintoul 2007) and gas giants (Porco et al. 2003). Thus the results of the present study warrant an assessment of large-scale kinetic-to-potential energy conversion in reanalysis products and observations. We also plan to assess the relevance of large-scale kinetic-to-potential energy conversion in Southern Ocean jets, which depend on topography, time and changes in forcing (Thompson & Richards 2011; Klocker 2018; Khatri & Berloff 2018).

In § 3.3 we connected the energy diagnostic terms to the physical processes that support energy conversion between EAPE and BC EKE. We also showed that the energy diagnostic associated with linear barotropisation is dependent on a term (background advection of BT vorticity) that supports vertical velocities that convert EAPE to BC EKE at the deformation scale. This result suggests a mechanism for the direct conversion of EAPE to BT EKE. An important caveat is that energy budgets, although a powerful means of interpretation, are not a definitive means of inferring fundamental physics (Lorenz 1955; Plumb 1983;

## M. Lobo

Bleck 1985). Thus further work will be aimed at alternate methods for characterising the BC energy pathways highlighted in this study, such as the coarse-graining approach (Eyink & Aluie 2009; Aluie, Hecht & Vallis 2018) or a framework of spatio-temporal energy fluxes (Mondal *et al.* 2025).

Both rough bottom topography (Pudig & Smith 2025) and a sloping bottom (Sterl *et al.* 2025; Lobo & Griffies 2025) affect the development and equilibration of two-layer QG turbulence in a drag-dependent fashion. Unlike planetary  $\beta$ , a meridionally sloping bottom mediates transfers of energy between the BT and BC modes, dependent on the sign of the bottom slope (Deng & Wang 2024). Current research efforts are aimed at defining the context of the present results in systems with bottom topography, using both the two-layer QG model and more comprehensive models. In addition, any results that rely on frictional energisation of the BC mode might manifest as bottom-intensified processes (e.g. Swaters 2009; Stewart & Thompson 2016), rather than full-column processes, as is implicit in the use of a two-layer QG model. Last, some of the phenomenological explanations of the present study rely on linear bottom friction. It is worthwhile to see whether these results extend to simulations with quadratic bottom friction.

Acknowledgements. I thank S.M. Griffies, R. Barkan, I. Held, K.S. Smith, M. Pudig, M. Sterl and W. Zhang for insightful discussion, and S.M. Griffies for very helpful comments on an earlier version of the manuscript. I also thank A. Thompson and two anonymous reviewers for comments that greatly improved the clarity and potential impact of the manuscript. Last, I thank the editor, Professor L.-P. Wang, for facilitating an efficient and enjoyable review process. Computational resources were provided by the Princeton Institute for Computational Science and Engineering, a resource of the Cooperative Institute for Modeling the Earth System.

Funding. This work was funded by NOAA award number NA23OAR4320198.

**Declarations of interests.** The author declares no competing interests.

**Data availability statement.** All code required to replicate the simulations, analysis and figures is published at https://github.com/mjclobo/JFM\_BC\_nrg\_cycles.

## REFERENCES

ALUIE, H., HECHT, M. & VALLIS, G.K. 2018 Mapping the energy Cascade in the North Atlantic ocean: the coarse-graining approach. *J. Phys. Oceanogr.* 48 (2), 225–244.

ARBIC, B.K. & FLIERL, G.R. 2004 Baroclinically unstable geostrophic turbulence in the limits of strong and weak bottom Ekman friction: application to midocean eddies. *J. Phys. Oceanogr.* **34** (10), 2257–2273.

BERLOFF, P., KARABASOV, S., FARRAR, J.T. & KAMENKOVICH, I. 2011 On latency of multiple zonal jets in the oceans. *J. Fluid Mech.* **686**, 534–567.

BLECK, R. 1985 On the conversion between mean and eddy components of potential and kinetic energy in isentropic and isopycnic coordinates. *Dyn. Atmos. Oceans* **9** (1), 17–37.

CHARNEY, J. 1947 The dynamics of long waves in a Baroclinic westerly current. J. Meteorol. 4 (5), 135–162.
CHARNEY, J.G. & ELIASSEN, A. 1949 A numerical method for predicting the perturbations of the middle latitude westerlies. Tellus 1 (2), 38–54.

CONNAUGHTON, C., NAZARENKO, S. & QUINN, B. 2015 Rossby and drift wave turbulence and zonal flows: The Charney–Hasegawa–Mima model and its extensions. *Phys. Rep.* **604**, 1–71.

CONSTANTINOU, N., WAGNER, G., SIEGELMAN, L., PEARSON, B. & PALÓCZY, A. 2021 GeophysicalFlows.jl: Solvers for geophysical fluid dynamics problems in periodic domains on CPUs GPUs. *J. Open Source Software* 6 (60), 3053.

DENG, P. & WANG, Y. 2024 Distinct impacts of topographic versus planetary PV gradients on baroclinic turbulence. *J. Phys. Oceanogr.* **54**, 2205–2231.

DETTMER, J. & EDEN, C. 2025 Mechanisms of baroclinic eddy damping on large scales. *J. Phys. Oceanogr.* 55 (10), 1751–1769.

EADY, E.T. 1949 Long waves and cyclone waves. Tellus 1 (3), 33-52.

EYINK, G.L. & ALUIE, H. 2009 Localness of energy cascade in hydrodynamic turbulence. I. Smooth coarse graining. *Phys. Fluids* 21 (11), 115107.

- FERRARI, R. & NIKURASHIN, M. 2010 Suppression of eddy diffusivity across jets in the southern ocean. J. Phys. Oceanogr. 40 (7), 1501–1519.
- FERRARI, R. & WUNSCH, C. 2009 Ocean circulation kinetic energy: reservoirs, sources, and sinks. *Annu. Rev. Fluid Mech.* **41** (2009), 253–282.
- GALLET, B. & FERRARI, R. 2020 The vortex gas scaling regime of baroclinic turbulence. Proc. Natl Acad. Sci. 117 (9), 4491–4497.
- HASEGAWA, A., MACLENNAN, C.G. & KODAMA, Y. 1979 Nonlinear behavior and turbulence spectra of drift waves and Rossby waves. *Phys. Fluids* 22 (11), 2122–2129.
- Held, I.M. & Larichev, V.D. 1996 A scaling theory for horizontally homogeneous, Baroclinically unstable flow on a beta plane. *J. Atmos. Sci.* 53 (7), 946–952.
- HOLLOWAY, G. & KRISTMANNSSON, S.S. 1984 Stirring and transport of tracer fields by geostrophic turbulence. J. Fluid Mech. 141, 27–50.
- HOSKINS, B., PEDDER, M. & JONES, D.W. 2003 The omega equation and potential vorticity. Q. J. Roy. Meteor. Soc. 129 (595), 3277–3303.
- HOSKINS, B.J., DRAGHICI, I. & DAVIES, H.C. 1978 A new look at the ω-equation. Q. J. Roy. Meteor. Soc. 104 (439), 31–38.
- JANSEN, M.F. & HELD, I.M. 2014 Parameterizing subgrid-scale eddy effects using energetically consistent backscatter. Ocean Model. 80, 36–48.
- JOUGLA, T. & DRITSCHEL, D.G. 2017 On the energetics of a two-layer Baroclinic flow. J. Fluid Mech. 816, 586–618.
- KHATRI, H. & BERLOFF, P. 2018 A mechanism for jet drift over topography. J. Fluid Mech. 845, 392–416.
- KLOCKER, A. 2018 Opening the window to the southern ocean: the role of jet dynamics. Sci. Adv. 4 (10), eaao4719.
- LACASCE, J.H. 1996 Baroclinic vortices over a sloping bottom. Phd thesis, Massachusetts Institute of Technology
- LARICHEV, V.D. & HELD, I.M. 1995 Eddy Amplitudes and fluxes in a homogeneous model of fully developed Baroclinic instability. J. Phys. Oceanogr. 25 (10), 2285–2297.
- LEE, S. 1997 Maintenance of multiple jets in a Baroclinic flow. J. Atmos. Sci. 54 (13), 1726-1738.
- LEE, S. 2010 Dissipative energization of baroclinic waves by surface Ekman pumping. *J. Atmos. Sci.* **67** (7), 2251–2259.
- LI, H. & XU, Y. 2021 Barotropic and Baroclinic inverse kinetic energy Cascade in the Antarctic circumpolar current. J. Phys. Oceanogr. 51 (3), 809–824.
- LOBO, M. & GRIFFIES, S.M. 2025 Two-Layer Quasi-Geostrophic Waves and Turbulence over a Meridionally Sloping Bottom with Linear Bottom Drag. Authorea Preprints.
- LOBO, M., GRIFFIES, S.M. & ZHANG, W. 2025 Vertical structure of Baroclinic instability in a three-layer quasigeostrophic model over a sloping bottom. *J. Phys. Oceanogr.* **55** (4), 341–359.
- LORENZ, E.N. 1955 Available potential energy and the maintenance of the general circulation. *Tellus* 7 (2), 157–167.
- MAXIMENKO, N.A., BANG, B. & SASAKI, H. 2005 Observational evidence of alternating zonal jets in the world ocean. *Geophys. Res. Lett.* **32** (12), 1–4.
- MONDAL, A., MORTEN, A.J., ARBIC, B.K., FLIERL, G.R., SCOTT, R.B. & SKITKA, J. 2025 Spatiotemporal spectral transfers in fluid dynamics. *Phys. Rev. Fluids* 10, 064602.
- PANETTA, R.L. 1993 Zonal jets in wide baroclinically unstable regions: persistence and scale selection. J. Atmos. Sci. 50 (14), 2073–2106.
- PANETTA, R.L., HELD, I.M. & PIERREHUMBERT, R.T. 1987 External Rossby waves in the two-layer model. J. Atmos. Sci. 44 (20), 2924–2933.
- PINOT, J.-M., TINTORÉ, J. & WANG, D.-P. 1996 A study of the omega equation for diagnosing vertical motions at ocean fronts. *J. Mar. Res.* 54 (595), 239–259.
- PLUMB, R.A. 1983 A new look at the energy cycle. J. Atmos. Sci. 40 (7), 1669–1688.
- PORCO, C.C., *et al.* 2003 Cassini imaging of jupiter's atmosphere, satellites, and rings. *Science* **299** (5612), 1541–1547.
- PUDIG, M.P. & SMITH, K.S. 2025 Baroclinic turbulence above rough topography: the vortex gas and topographic turbulence regimes. *J. Phys. Oceanogr.* 55, 611–630.
- RHINES, P.B. 1994 Jets. Chaos: An Interdisciplinary J. Nonlinear Sci. 4 (2), 313–339.
- ROSSBY, C.-G. 1939 Relation between variations in the intensity of the zonal circulation of the atmosphere and the displacements of the semi-permanent centers of action. *J. Mar. Res.* 2 (1), 38–55.
- ROULLET, G., MCWILLIAMS, J.C., CAPET, X. & MOLEMAKER, M.J. 2012 Properties of steady geostrophic turbulence with isopycnal outcropping. *J. Phys. Oceanogr.* **42** (1), 18–38.
- SALMON, R. 1980 Baroclinic instability and geostrophic turbulence. Geophys. Astrophys. Fluid Dyn. 15 (1), 167–211.

## M. Lobo

- SCOTT, R.B. & ARBIC, B.K. 2007 Spectral energy fluxes in geostrophic turbulence: implications for ocean energetics. *J. Phys. Oceanogr.* **37** (3), 673–688.
- SCOTT, R.B. & WANG, F. 2005 Direct evidence of an oceanic inverse kinetic energy cascade from satellite altimetry. *J. Phys. Oceanogr.* **35** (9), 1650–1666.
- SMITH, K.S. 2005 Tracer transport along and across coherent jets in two-dimensional turbulent flow. *J. Fluid Mech.* **544**, 133–142.
- SMITH, K.S. & VALLIS, G.K. 2002 The scales and equilibration of midocean eddies: forced–dissipative flow. J. Phys. Oceanogr. 32 (6), 1699–1720.
- SOKOLOV, S. & RINTOUL, S.R. 2007 Multiple jets of the Antarctic circumpolar current south of Australia. J. Phys. Oceanogr. 37 (5), 1394–1412.
- STERL, M.F., PALÓCZY, A., GROESKAMP, S., BAATSEN, M.L.J., LACASCE, J.H. & ISACHSEN, P.E. 2025 The joint effects of planetary *eta*, topography and friction on baroclinic instability in a two-layer QG model. *Authorea Preprints*.
- STEWART, A.L. & THOMPSON, A.F. 2016 Eddy generation and jet formation via dense water outflows across the antarctic continental slope. *J. Phys. Oceanogr.* **46** (12), 3729–3750.
- STORER, B.A., BUZZICOTTI, M., KHATRI, H., GRIFFIES, S.M. & ALUIE, H. 2023 Global cascade of kinetic energy in the ocean and the atmospheric imprint. *Sci. Adv.* 9 (51), eadi7420.
- SWATERS, G.E. 2009 Ekman destabilization of inertially stable baroclinic abyssal flow on a sloping bottom. Phys. Fluids 21 (8), 086601.
- THOMPSON, A.F. 2010 Jet formation and evolution in Baroclinic turbulence with simple topography. *J. Phys. Oceanogr.* **40** (2), 257–278.
- THOMPSON, A.F. & RICHARDS, K.J. 2011 Low frequency variability of southern ocean jets. *J. Geophys. Res. Oceans* **116** (C9), 1–17.
- THOMPSON, A.F. & YOUNG, W.R. 2006 Scaling Baroclinic eddy fluxes: vortices and energy balance. *J. Phys. Oceanogr.* **36** (4), 720–738.
- THOMPSON, A.F. & YOUNG, W.R. 2007 Two-layer Baroclinic eddy heat fluxes: zonal flows and energy balance. *J. Atmos. Sci.* **64** (9), 3214–3231.
- VALLIS, G.K. 2017 Atmospheric and Oceanic Fluid Dynamics. 2nd edn. Cambridge University Press.
- VALLIS, G.K. & MALTRUD, M.E. 1993 Generation of mean flows and jets on a beta plane and over topography. *J. Phys. Oceanogr.* 23 (7), 1346–1362.
- VENAILLE, A., VALLIS, G.K. & GRIFFIES, S.M. 2012 The catalytic role of the beta effect in barotropization processes. J. Fluid Mech. 709, 490–515.
- WANG, L., JANSEN, M. & ABERNATHEY, R. 2016 Eddy phase speeds in a two-layer model of quasigeostrophic Baroclinic turbulence with applications to ocean observations. *J. Phys. Oceanogr.* 46 (6), 1963–1985.
- WANG, S., JING, Z., ZHANG, Q., CHANG, P., CHEN, Z., LIU, H. & WU, L. 2019 Ocean eddy energetics in the spectral space as revealed by high-resolution general circulation models. *J. Phys. Oceanogr.* **49** (11), 2815–2827.
- WILLIAMS, P. 1985 Jovian and comparative atmospheric modeling gareth. In *Issues in Atmospheric and Oceanic Modeling*, (ed. B. Saltzman) Advances in Geophysics, vol. 28, pp. 381–429. Elsevier
- YOUNG, R. & READ, P. 2017 Forward and inverse kinetic energy cascades in Jupiter's turbulent weather layer. Nat. Phys. 13, 1135–1140.